Check for updates

Experimental study of the effect of CO$_2$ on temperature and soot volume fraction in C$_2$H$_4$/air co-flow laminar diffusion flame

Xiuli An, Weiguang Cai, Yu Yang, Shu Zheng* and Qiang Lu ![ORCID]*

The threat of global warming caused by greenhouse gases such as CO$_2$ to the environment is one of the most intractable challenges. The capture and utilization of CO$_2$ are essential to reduce its emission and achieve the goal of being carbon neutral, in which CO$_2$-diluted combustion is an efficient carbon capture technology. In this research, the effects of CO$_2$ addition in the fuel side (CO$_2$–F), oxidizer side (CO$_2$–O) and both sides (CO$_2$–F/O) on temperature and soot formation in C$_2$H$_4$/air laminar co-flow diffusion flames were researched. The flame images were measured by a complementary metal-oxide-semiconductor (CMOS) imaging equipment. The two-dimensional distributions of temperature and soot volume fraction in C$_2$H$_4$/air laminar co-flow diffusion flames were measured employing the inverse Abel transform. The results demonstrated that the effect of amount variation of CO$_2$–F on the decrease of flame temperature was enhanced by the CO$_2$–O. The reduction in peak flame temperature was 4 K in the CO$_2$–F cases, while the reduction in peak flame temperature was 83 K in the CO$_2$–F/O cases. The soot formation was suppressed significantly by the effects of CO$_2$–F/O. Compared with the CO$_2$–F cases, the reductions in peak soot volume fraction were 22.5% and 23.5% in the CO$_2$–F/O cases. The suppression effect of amount variation of the CO$_2$–F on soot formation became more significant with the increase of flame height. The reductions in peak soot volume fractions were 0.3%, 3.07% and 6.38% at the flame heights of 20 mm, 30 mm and 40 mm in the CO$_2$–F cases, and the corresponding reductions were 4.92%, 5.2% and 16% in the CO$_2$–F/O cases, respectively.

1. Introduction

With the intensified global warming, carbon peaking and carbon neutrality as the key strategies to mitigate climate change, have attracted widespread attention.[1,2] Various low-emission combustion technologies have been developed to achieve this goal.[3–5] The common characteristic of these technologies is to employ the combustion product CO$_2$ to dilute the fuel and/or the oxidizer in order to achieve lean-burn conditions, such as the exhaust gas recirculation (EGR) technology[3] and the flue gas recirculation (FGR) technology.[6–8]

During the combustion process, the transfer process of heat and mass in the flame and soot formation are affected by CO$_2$ through physical and chemical interactions.[9–15] Hence, the employment of CO$_2$ as the dilution gas[12] is able to reduce the flame temperature and achieve low emission of pollutants. For CO$_2$–F, various conclusions were drawn on the suppression mechanism of soot formation in early research studies. Schug *et al.*[11] proved the effect of the CO$_2$–F on the reduction of soot formation was a purely thermal effect. Du *et al.*[16] carried out an

array of researches for the purpose of distinguishing the different effects of CO$_2$. The experiments proved that oxidation process of soot precursor was dominant by the chemical effects of CO$_2$, resulting in inhibition on soot formation. Subsequently, the fictitious CO$_2$ was introduced by Liu *et al.*[17] in the C$_2$H$_4$/CO$_2$ co-flow diffusion flame. The numerical study findings revealed that soot inception was suppressed by the C$_2$H$_2$ concentration reduction and the increase of OH radical concentration which caused by the CO$_2$–F. The chemical effect of CO$_2$ was dominated by the reaction of CO + OH = CO$_2$ + H. Gulder *et al.*[18] analyzed the soot formation path and the effect of CO$_2$ on each step of soot formation path. The numerical studies proved that the soot oxidation process was enhanced owing to the CO$_2$–F, leading to the suppression on soot formation. Based on the revised soot formation model, Frenklach *et al.*[19] proved that H radicals activating the radical sites on PAHs were reduced by the reaction of CO$_2$ + H = CO + OH, leading to a suppression on the H-abstraction-C$_2$H$_2$-addition (HACA) mechanism in soot particle inception and surface growth.

For the CO$_2$–O, its effect on flame temperature is usually more significant than that of the CO$_2$–F. Liu *et al.*[20] numerically simulated the two-dimensional temperature distributions in a C$_2$H$_4$ diffusion flame, the experimental results revealed that the reduction of flame temperature was 55 K attributed to the

National Engineering Research Center of New Energy Power Generation, North China Electric Power University, Beijing 102206, China. E-mail: shuzheng@ncepu.edu.cn; qianglu@mail.ustc.edu.cn

CO_2–O, which was larger than the reduction of 7 K attributed to the CO_2–F. Guo et al.[21] confirmed that the reduction of peak soot volume fraction in a laminar diffusion flame was 52.5% in the 50% CO_2–F, which was significantly less than that caused by the 50% CO_2–O (87.2%),[22] demonstrating that the suppression effects of CO_2–O on soot formation was different from that of CO_2–F.

The accurate measurements on soot volume fraction and flame temperature play a remarkable role in depth revealing the impact of CO_2 on soot formation. The laser spectrum detection has been employed in the combustion diagnosis, the high precision measurements of soot volume fraction can be achieved via the light extinction (LE) technology,[23–25] and laser-induced fluorescence (LIF) technology.[23–25] The soot volume fraction in the C_2H_4 counterflow diffusion flame was calculated by Wang et al.[26] employing the LE technology. The experimental studies proved that the decrease of soot volume fraction was 25.2% with 20% CO_2–F. M. Sirignano et al.[27] revealed that the decrease in soot volume fraction was 65% with the CO_2–O using the LIF technology. In addition, Liu et al.[28] employed the LIF technology to study the effect of CO_2–F on soot formation in the C_2H_4 flames. The experimental studies showed that the inhibition of CO_2 on soot formation was manifested in the inhibition of polycyclic aromatic hydrocarbons (PAHs). While Ying et al.[29] employed the CO_2 as oxidant to research the evolution of micro–nano structure and the reactivity of soot at the initial stage of C_2H_4 diffusion flames, and concluded that the sizes of primary particles was reduced by the CO_2–O, which led to the inhibition on soot formation mainly through the nucleation process instead of the PAHs process. The soot volume fraction measurement results obtained by the LE and the LIF technologies were the single-point results in line-of-sight direction, which was not enough for the study on the distributions of spatial of soot volume fraction. Many scholars have committed to accurately measure the two-dimensional distributions of soot volume fraction based on flame spontaneous emission.[30] Liu et al.[31] experimentally researched the suppression mechanism of the CO_2–F on the soot formation. The findings revealed that the reduction of peak soot volume fraction was 28.75% with thermal effect and 33.25% with chemical effect, which indicated that both the thermal effect and chemical effect of the CO_2–F had the notable suppression on the soot formation. Bowen et al.[32] combined the inverse Abel transform and CCD imaging technology to reconstruct the distributions of soot volume fraction in an O_2/CO_2 co-flow laminar diffusion flame, so as to exploring the effects of CO_2, the main diluent in flue gas recirculation technology, on soot formation. The results proved that the peak soot volume fraction reduced by 48.2% when the N_2 was replaced by CO_2 in the oxidizer side, larger than that of 16% with the N_2 adding in the oxidizer side, indicating that the suppression mechanism on soot formation was dominated by the chemical effect of the CO_2–O.

As summarized above, a remarkable difference occurred in the suppression effect and mechanism of CO_2–F and CO_2–O on soot formation. Currently, the internal flue gas recirculation technology was introduced to preheat and dilute reactants simultaneously on the fuel side and oxidizer side, aiming to reduce the release of pollutants on the basic of traditional external flue gas recirculation technology.[33] The coupling mechanism of CO_2–F/O on flame structure and soot formation and the difference in soot suppression among the CO_2–F, CO_2–O and CO_2–F/O were necessary to explore.

In this study, the two-dimensional distributions of temperature and soot volume fraction in CO_2-diluted C_2H_4 laminar co-flow diffusion flames were reconstructed experimentally by inverse Abel transform, based on the radiation intensity obtained by a calibrated complementary metal-oxide-semiconductor (CMOS) imaging equipment. This research is mainly different from previous studies by choosing CO_2–F/O as CO_2 addition mode instead of CO_2–F or CO_2–O. The organization of this paper was as follows. First, the combustion experimental system, the CMOS imaging equipment and the measurement methodology were described in Section 2. Subsequently, the reconstruction results of flame temperature and soot volume fraction were analyzed in Section 3. Finally, the main findings were summarized in the conclusions.

2. Experimental set-up and methodology

2.1 Experimental instrument

In this experiment, the bench of hydrocarbon fuel laminar diffusion combustion was employed, which could implement the researches of low-emission combustion. The combustion experiment system was shown in Fig. 1. The CO_2-diluted C_2H_4 co-flow laminar diffusion flames were generated by a Gülder type burner. The diameters of the outer and inner of the fuel tube were 12.8 mm and 10.9 mm, respectively. The oxidizer nozzle diameters were 88 mm (inner) and 100 mm (outer), respectively. Fuel flow passed through the central tube, the oxidizer passed through glass beads and porous metal disks to obtain a uniform mixture of oxidizer flow. All gases were delivered at 293 K and the air was dried by a refrigeration dryer. A fiber spectrometer (type: AvaSpec-Mini2048CL) with the wavelength range from 200–1100 nm was used to measure the flame radiation intensity at different heights of the flame. The
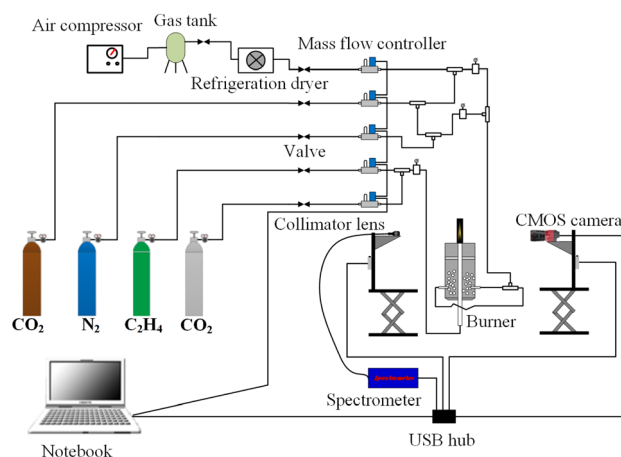

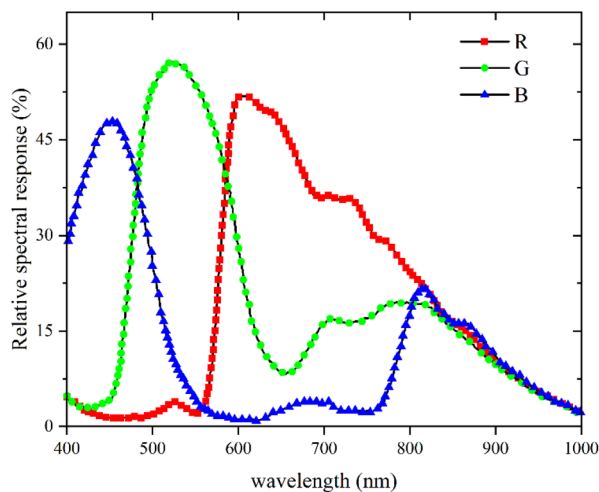Fig. 1 Schematic diagram of the combustion experiment system.

Fig. 2 Spectral response curves of the R, G and B bands of the CMOS imaging equipment.

flame was imaged by a CMOS imaging equipment (type: Alvium 1800 U-040c) with a pixel area of 6.9 μm × 6.9 μm and the resolution of 728 (H) × 544 (V) pixels. In order to ensure the flame brightness images were not affected by the random noise, the white balances of the R and G bands of the CMOS imaging equipment as set to 1.0 respectively. The central wavelengths were 610 nm, 535 nm and 430 nm for R, G and B imaging equipment as shown in Fig. 2. Since the chemiluminescent emission of the CH radical at 430 nm had radiative attribution to the B band of the CMOS imaging equipment, especially in the hydrocarbon flames, and the signal of B band was dramatically affected by the random noise, the flame spontaneous radiation measured by CMOS imaging equipment of R and G bands were employed to reconstruct the flame temperature and soot volume fraction distributions. In order to measure the high-quality color images of the flame, the CMOS imaging equipment was translated along the height of flame by the lift platform, then the complete flame images were obtained by the image processing technology.

The CMOS imaging equipment was a photoelectric conversion device. The flame images collected by the CMOS imaging equipment were the flame brightness data. The relationship between the flame brightness data and the flame radiation intensity was established by calibrating the CMOS imaging equipment employing a blackbody furnace. The temperature range of the blackbody furnace was 300 °C to 1700 °C and the uncertainty of the temperature was 0.25% of reading ±1 °C. To eliminate the impact of exposure time on the flame brightness data measured by CMOS imaging equipment, the quotient of flame brightness data and the exposure time was employed as the relative radiation intensity. Since the differences between the relative radiation intensity and the raw data obtained by R and G bands of the CMOS imaging equipment were significant large, in order to obtain the calibration results of the CMOS imaging equipment with high-precision, the relationship of the $\log(I_b R)$ and $\log(I_b G)$ with $\log(R/t)$ and $\log(G/t)$ was established, instead of the $I_b R$ and $I_b G$ with the flame brightness data of R
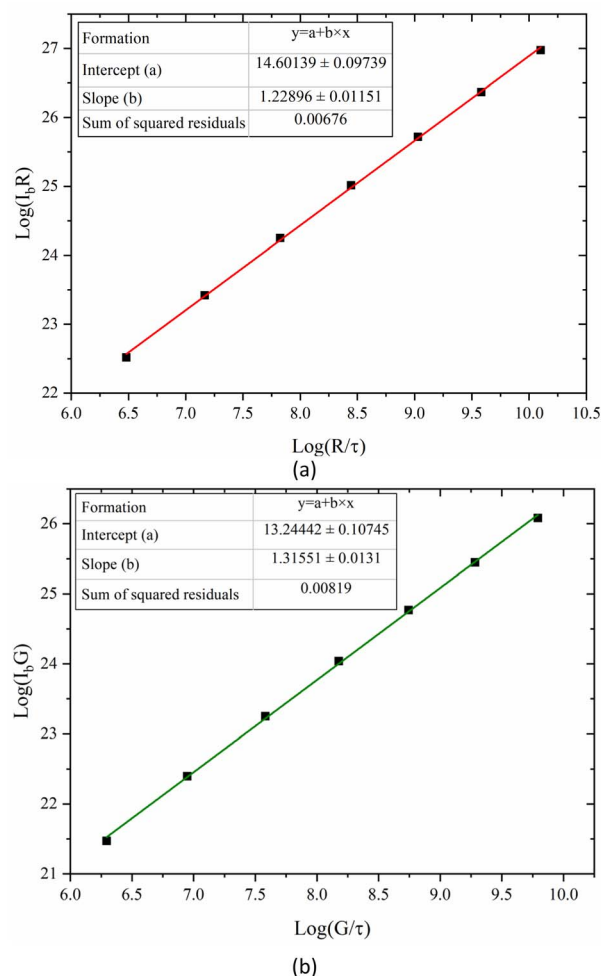

Fig. 3 Variation of (a) log(I_bR) and (b) log(I_bG) with log(R/t) and log(G/t).

and G bands. The variation of $\log(I_b R)$ and $\log(I_b G)$ with $\log(R/t)$ and $\log(G/t)$ was shown in Fig. 3. The scatters in the Fig. 3 were the flame brightness data and the absolute radiation intensity obtained by the blackbody furnace, and the lines in the Fig. 3 were the linear fitting of the scatter data. The relative radiation intensity and the absolute blackbody radiation intensity were the linear relationship of $\log(I_b R) = a + b \times \log(R/t)$ with the sum of the squared residuals of 0.007 and 0.008, respectively. The intercept a and the slope b represented the calibration coefficients. The intercepts were 14.60 and 13.24 for R and G bands, and the slopes were 1.23 and 1.32 for R and B bands, respectively.

In order to testify the accuracy of the calibration of CMOS imaging equipment, the $I_{\lambda R}$ and $I_{\lambda G}$ with setting temperatures of blackbody furnace from 1073 K to 1623 K at the interval of 50 K were recalculated employing the calibration coefficients. The calibration temperatures were calculated by the two-color method and the recalculated $I_{\lambda R}$ and $I_{\lambda G}$, and compared with the blackbody furnace setting temperatures. The calibration results were shown in Table 1. The maximum relative calibration errors were 0.94% and 1.31% for $I_{\lambda R}$ and $I_{\lambda G}$, respectively, and the maximum relative error of the calibration temperature was 0.48%, indicating that the calibration process was accurate.

Table 1 The results of blackbody furnace calibration[a]

T_b (K)	$I_{\lambda R}$ (W m^{-3} sr^{-1})	$I_{\lambda R}^{error}$ (%)	$I_{\lambda G}$ (W m^{-3} sr^{-1})	$I_{\lambda G}^{error}$ (%)	T_c (K)	T_c^{error} (%)	ε_c
1073	4.04×10^5	0.94	3.57×10^4	0.95	1074	0.003	1.01
1123	1.07×10^6	0.24	1.09×10^5	0.95	1126	0.24	1.05
1173	2.61×10^6	0.14	3.03×10^5	1.15	1177	0.36	1.07
1223	5.95×10^6	0.29	7.67×10^5	0.19	1222	0.04	0.99
1273	1.27×10^6	0.11	1.82×10^5	0.25	1274	0.05	1.05
1323	2.56×10^6	0.31	4.08×10^5	1.05	1327	0.29	1.05
1373	4.92×10^7	0.81	8.55×10^6	1.15	1374	0.01	1.02
1423	8.98×10^7	0.61	1.69×10^7	0.05	1419	0.24	0.96
1473	1.57×10^8	0.10	3.22×10^7	0.75	1477	0.29	1.05
1523	2.67×10^8	0.59	5.88×10^7	1.01	1526	0.19	1.03
1573	4.35×10^8	0.29	1.04×10^8	1.31	1580	0.48	1.07
1623	6.91×10^8	0.49	1.74×10^8	0.71	1625	0.11	1.02

[a] T_b represented the setting temperature of blackbody furnace, $I_{\lambda R}$ and $I_{\lambda G}$ represented the measured radiation intensities of R and G bands, $I_{\lambda R}^{error}$ and $I_{\lambda G}^{error}$ (%) represented the relative errors of the measured radiation intensities, T_c and T_c^{error} represented the calculated temperature and the relative error of calculated temperature, respectively, ε_c represented the calculated emissivity.

Four different experimental conditions were tested, as summarized in Table 2. The flow rates of C_2H_4 and air were 150 mL min^{-1} in fuel side and 40 L min^{-1} in the oxidizer side, respectively. For the case 1 and the case 2, the flow rates of CO_2 were 20% and 30% of C_2H_4 flow rate in the fuel side, respectively.

The two the cases were employed to explore the effects of amount variation of the CO_2–F on flame temperature and soot volume fraction. On the basis of the case 1 and the case 2, the CO_2 with the flow rate of 10% of air flow rate was added in the oxidizer side, to explore the effects of CO_2–F/O on flame temperature and soot formation for the case 3 and the case 4.

2.2 Methodology principle

The measured flame with a cross-section radius of R_f was divided into N concentric rings as shown in Fig. 4. N was depended on the resolution of the CMOS imaging equipment in this experimental research. The accumulation of the radiation intensity emitted by the concentric rings passing through line-of-sight was received by the CMOS imaging equipment. L_{CMOS} represented the distance between the imaging equipment and the central axis of flame. The flame was in the angular field of view of the CMOS imaging equipment. The calculating angle field was $\theta \in [-\theta_f, \theta_f]$, where $\theta_f = \arcsin(R_f/L_{CMOS})$. θ_j was the included angle between the j line of the sight of the CMOS imaging equipment and the x-axis.

With optically thin assumption, the spectral radiation intensity $I_\lambda(j)$ received from the j line can be written as:

$$I_\lambda(j) = \int_{l_0(j)}^{l_i(j)} \kappa_\lambda(l) I_{b\lambda}(l) dl = \int_{l_0(j)}^{l_i(j)} H_\lambda(l) dl \quad (1)$$

where l was the path of the radiation intensity, $H(\lambda)$ the emission source term, λ the wavelength, I_b the blackbody radiation intensity of soot according to Plank's law as follows:

$$I_b = \frac{c_1}{\lambda^5(e^{c_2/(\lambda T)} - 1)\pi} \quad (2)$$

where c_1 and c_2 were the Plank's constants, κ_λ the spectral absorption coefficient of soot particles, and expressed according to the Rayleigh approximation:[31,34]

$$\kappa_\lambda(l) = \frac{6\pi E(m) f_v(l)}{\lambda} \quad (3)$$

where $E(m)$ was the complex function of the refractive index m, which can be expressed as $m = 1.57 + 0.56i$,[35,36] f_v the soot volume fraction.

The R and G raw data of flame measured by the CMOS imaging equipment were assumed approximately to be the proportional to the monochromatic radiative intensities of the R and G bands in the previous researches. However, the spectral response spectrums of the CMOS imaging equipment were
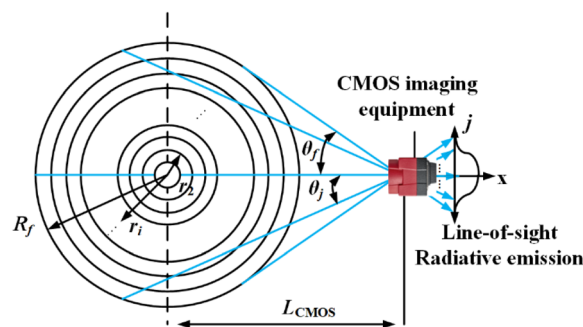
Table 2 Experimental conditions

	Fuel side (mL min^{-1})		Oxidizer side (L min^{-1})	
Case	C_2H_4	CO_2	Air	CO_2
Case 1	150	30	40	0
Case 2	150	45	40	0
Case 3	150	30	40	4
Case 4	150	45	40	4

Fig. 4 Schematic diagram of flame horizontal section measurement.

board, as shown in Fig. 2. To obtain the real brightness data in the R and G bands of the CMOS imaging equipment. The spectral response values of R and G bands were described by the functions of the wavelength $\sim \eta_R$, η_G, and the directional transmission power E_R and E_G can be expressed as follows:

$$E_R(j) = \int_{\lambda_{R1}}^{\lambda_{R2}} \eta_{R,l} I_l(j)\,dl = \int_{l_0(j)}^{l_1(j)} \int_{\lambda_{R1}}^{\lambda_{R2}} \eta_{R,\lambda}\kappa_\lambda(l)I_{b\lambda}(l)\,d\lambda dl$$

$$= \int_{l_0(j)}^{l_1(j)} H_R(j)\,dl$$

$$E_G(j) = \int_{\lambda_{G1}}^{\lambda_{G2}} \eta_{G,l} I_l(j)\,dl = \int_{l_0(j)}^{l_1(j)} \int_{\lambda_{G1}}^{\lambda_{G2}} \eta_{R,\lambda}\kappa_\lambda(l)I_{b\lambda}(l)\,d\lambda dl$$

$$= \int_{l_0(j)}^{l_1(j)} H_G(j)\,dl \tag{4}$$

where η_R and η_G were the spectral response values.

According to the inversion algorithm, the local emission source terms H_R and H_G were solved by eqn (5):

$$
\begin{bmatrix} E_R(1) \\ E_R(j) \\ \vdots \\ E_R(M) \end{bmatrix} =
\begin{bmatrix}
\Delta l_{1,1} & \cdots & \Delta l_{1,N-1} & \Delta l_{1,N} \\
0 & \Delta l_{j,i} & \cdots & \Delta l_{2,N} \\
\vdots & \vdots & \vdots & \vdots \\
\cdots & \cdots & \cdots & \Delta l_{M,N}
\end{bmatrix} \cdot
\begin{bmatrix} H_R(1) \\ H_R(2) \\ \vdots \\ H_R(N) \end{bmatrix}
$$

$$
\begin{bmatrix} E_G(1) \\ E_G(j) \\ \vdots \\ E_G(M) \end{bmatrix} =
\begin{bmatrix}
\Delta l_{1,1} & \cdots & \Delta l_{1,N-1} & \Delta l_{1,N} \\
0 & \Delta l_{j,i} & \cdots & \Delta l_{2,N} \\
\vdots & \vdots & \vdots & \vdots \\
\cdots & \cdots & \cdots & \Delta l_{M,N}
\end{bmatrix} \cdot
\begin{bmatrix} H_G(1) \\ H_G(2) \\ \vdots \\ H_G(N) \end{bmatrix}
\tag{5}
$$

The flame temperature was obtained by the ratio of H_R and H_G as follows:

$$\frac{H_R}{H_G} = \frac{\int_{\lambda_{R_1}}^{\lambda_{R_2}} \eta_{R,\lambda}\kappa_\lambda(l)I_{b\lambda}(l)\,d\lambda}{\int_{\lambda_{G_1}}^{\lambda_{G_2}} \eta_{G,\lambda}\kappa_\lambda(l)I_{b\lambda}(l)\,d\lambda}$$

$$= \frac{\int_{\lambda_{R_1}}^{\lambda_{R_2}} \eta_{R,\lambda}\dfrac{6\pi E(m)f_v(l)}{\lambda}\dfrac{c_1}{\lambda^5(e^{c_2/(\lambda T)}-1)\pi}\,d\lambda}{\int_{\lambda_{G_1}}^{\lambda_{G_2}} \eta_{G,\lambda}\dfrac{6\pi E(m)f_v(l)}{\lambda}\dfrac{c_1}{\lambda^5(e^{c_2/(\lambda T)}-1)\pi}\,d\lambda} \tag{6}$$

Finally, the soot volume fraction distributions can be reconstructed according to eqn (3).

3. Results and discussions

The color images of the measured flames from case 1 to case 4 were shown in Fig. 5. The flame height of the case 1 was 59.83 mm, which was slightly higher than that of 57.94 mm in the case 2. In the case 4, the flame height was 66.4 mm, which was
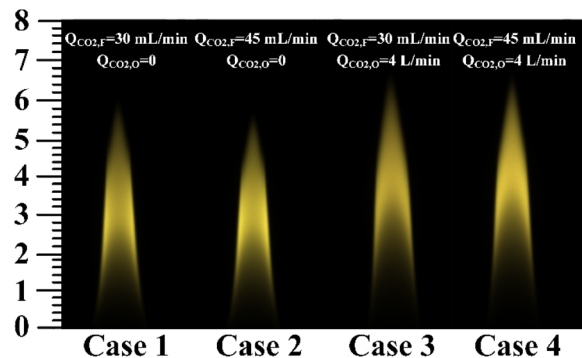

Fig. 5 Photographs of the flame shapes from case 1 to case 4.

slightly lower than that of the case 3 (67.74 mm). The height of flame decreased with the increase of the amount of CO_2–F. Compared with the case 1 and the case 2, the flame heights increased by 7.91 mm and 8.46 mm for the case 3 and the case 4, respectively, indicating that the CO_2–O led to the significant increase in flame height. The flame height was increased due to the density and transport effects of CO_2. For the density effect, the binary diffusion coefficient of the CO_2 and O_2 mixture was lower than that of the air, which weakened the oxygen diffusion process, and required the flame to develop to a higher place to burn completely. Due to the increase of the axial velocity in the oxidizer zone caused by the transport effect of CO_2–O, the oxidizer flowed through a longer distance in the same residence time. More fuel was transported by CO_2 to the top of the flame, resulting in an increase in flame height.

The reconstructed two-dimensional flame temperature distributions from the case 1 to the case 4 were shown in Fig. 6. Compared with the case 1 and the case 2, the peak flame temperatures decreased by 145 K and 224 K for the case 3 and
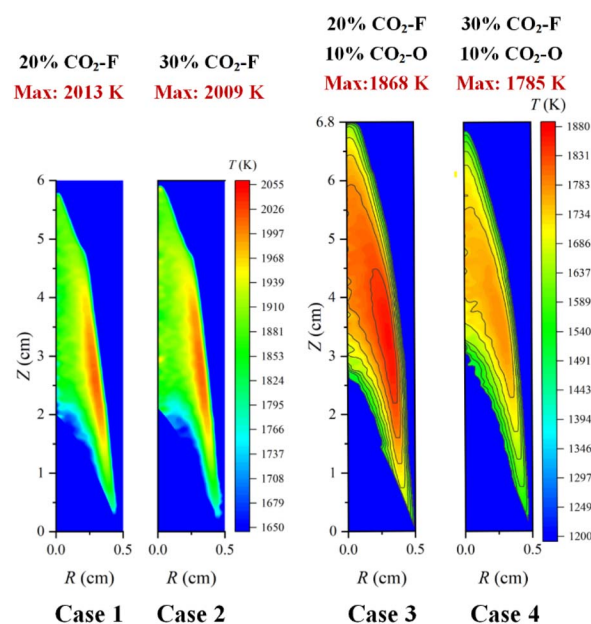

Fig. 6 The flame temperature distributions from case 1 to case 4.

the case 4, respectively, indicating that the decrease in flame temperature was caused by the CO_2–F/O. Compared with the case 3, the flame height decreased by 1.0 cm in the case 1 owing to the transport effect of CO_2. The oxygen diffusion process was weakened with the CO_2–O in the CO_2–F/O cases, because the CO_2 had a lower diffusion coefficient compared with the air, and a higher height of the flame was required for the complete burning. The temperatures at the center axis of flame increased from 1785 K in the case 1 to 1866 K in the case 2 at the flame height of 5.5 cm and the increase of 60 K from the case 1 to the case 2 which appeared at the flame center axis height of 2.9 cm, indicating that the effect of the CO_2–F on the decrease of flame temperature was mainly in the two wings region of the flame. The heights of the temperature first measured in the flame central axis were 2 cm along the direction of the fuel addition in the CO_2–F cases. However, the heights of the temperature first measured in the flame central axis increased to 2.5 cm and 3.2 cm along the direction of the fuel addition for the case 3 and the case 4, respectively, which indicated that the fuel combustion in the central axis region of the flame was affected by the CO_2–F/O.

The decrease in peak flame temperature was only 4 K with the amount of the CO_2–F increased from 20% to 30% in the CO_2–F cases, confirming the little effect of amount variation of the CO_2–F on the decrease of flame temperature. Whereas in the CO_2–F/O cases, the effect of amount variation of the CO_2–F on flame temperature became more significant with the peak flame temperatures decreasing from 1868 K to 1785 K, which was attributed to the thermal and chemical effects of CO_2. The thermal effect was that more heat was absorbed since the heat capacity of CO_2 was larger than that of air. For the chemical effect, the main endothermic chain branching reaction ($O + OH = H + O_2$) was enhanced due to the reduction of the H radical concentration *via* the reaction of $CO_2 + H = CO + OH$. The high flame temperature region in the CO_2–F cases (the height of 2.3–3.2 cm, the radius of 0.28–0.32 cm) was higher than that in the CO_2–F/O cases (the height of 3.5–3.8 cm, the radius of 0.32–0.34 cm), accompanied with the expanding of the region of high flame temperature to the two wings due to the CO_2–O. The reason was that the buoyancy of the oxidant gradually decreased with the CO_2–O, resulting in a decrease in the axial velocity of the fuel transport. The mixing time of the fuel and oxidant was delayed, and thus, the region of flame high temperature expanded to the oxidizer side.

Fig. 7 showed the soot volume fraction distributions from case 1 to case 4. The maximum soot volume fraction in the CO_2–F cases were 4.3×10^{-6} and 4.21×10^{-6}, respectively, existing in the flame co-annular zone with the height of $z = 3.5$ cm and the radius of 0.3 cm, higher than the height of co-annular region with peak flame temperature position. Compared with the case 1, the main region of soot formation (the height of 1.8–3.7 cm) was similar to the regions of soot formation for the case 2 and the case 3. Whereas, the height of soot formation main region increased to 2.2–4.25 cm for the case 4, which indicated that the increase of the height of soot formation region was achieved by the combined effects of the CO_2–F and CO_2–O. In the CO_2–F cases, the soot volume fraction distributions showed
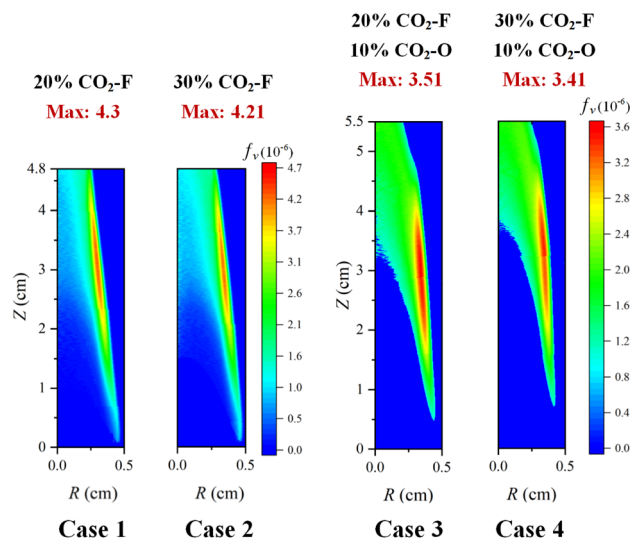

Fig. 7 The soot volume fraction distributions from case 1 to case 4.

a great difference outside the main region of soot formation. At the flame height of 4.3 cm, the soot volume fraction of the flame boundary was 3.16×10^{-6} for case 1 (the radius of 0.27 cm), which was 49% higher than that at the flame axis, while in the CO_2–F/O cases, the soot volume fraction distributions were almost the same outside the main region of soot formation, which the maximum and minimum soot volume fraction were 2.2×10^{-6} and 2.09×10^{-6}, respectively.

The amount variation of the CO_2–F had a slight influence on soot formation suppression for all cases. The reduction in soot volume fraction was 2.1% with the amount of the CO_2–F increasing from 20% to 30% in the CO_2–F cases, and the soot volume fraction reduction in the CO_2–F/O cases was 2.85%.

Compared with the case 1 and the case 2, the peak soot volume fractions reduced by 22.5% and 23.5% for the cases 3 and the case 4, respectively, indicating that the suppression of soot formation was affected significantly by the effects of CO_2–F/O. The soot formation could be described by the processes of nucleation and surface growth. The nucleation rate was proportional to the flame temperature. The flame temperature decreased with the dilution effect of CO_2–O. The molar mass of air was less than that of CO_2, so the oxidant density with CO_2–O was larger than that with air addition in the oxidizer side. In the oxidant zone away from the reaction flame, the increase of the buoyancy of the oxidizer, which caused by air was replaced by CO_2 led to an increase in the axial velocity in this area, reducing the mixing time between the fuel and oxidant flow, thus decreasing the combustion intensity and flame temperature. The substitution of oxygen by CO_2 resulted in a drop on the oxygen concentration, which decreased the flame temperature and suppressed the formation of soot. The flame temperature reduction caused by the CO_2–F/O led to the inhibition of the soot nucleation. The processes of surface growth could be described by the HACA and the condensation processes. The forward reaction rate of $CO_2 + H = CO + OH$ was promoted due to the CO_2–F/O, resulting in the decrease of H radical concentration, which consequently resulted in the reduction of active

sites in the process of the HACA. Similar to the soot nucleation process, the condensation rate was also proportional to the flame temperature. Therefore, the soot formation was suppressed owing to the decrease of nucleation and condensation rate as well as the inhibition of HACA process caused by the CO_2–F/O.

The nucleation rate and condensation rate magnitudes were shown in Fig. 8. For CO_2–F cases (case 1 and case 2), the reductions of nucleation rate and condensation rate were 3.99% and 7.82%, respectively, revealing that the processes of soot nucleation and condensation were suppressed with the amount of CO_2–F increasing from 20% to 30%. The reductions of nucleation and condensation rates were 21.18% and 20.54% for CO_2–F/O cases (case 3 and case 4), indicating that the CO_2–F/O was more effective on suppressing the processes of soot nucleation and condensation.

The distributions of flame temperature and soot volume fraction along the radius directional above the different heights (20 mm, 30 mm, and 40 mm) of the burner outlet were compared in Fig. 9. There was no significant difference for peak flame temperatures at different heights of the flame in the CO_2–F cases, but the position of peak flame temperature point of the case 1 was closer to the flame central axis compared with the case 2, which demonstrated that the chemical reaction region expanded to the two wings region with the amount of the CO_2–F increasing from 20% to 30%. It was evident that the flame temperature increased with the amount increase of the CO_2–F at the central axis area of the flame, while in other areas (except the regions near the oxidizer side), the flame temperature decreased in the CO_2–F cases. The coordinates of the demarcation points were 1.23 mm and 1.55 mm in radius, 30 mm and 40 mm in height as shown in the Fig. 9a and b, respectively. This phenomenon disappeared with the CO_2–F/O as shown in Fig. 9c. The flame temperatures of 20% CO_2–F were higher than those of 30% CO_2–F in the CO_2–F/O cases.

At the root of the flame (flame height of 20 mm), the CO_2–F did not exhibit significantly the inhibiting effect on soot formation in the CO_2–F cases. When the amount of the CO_2–F increased by 10%, the peak soot volume fraction was only reduced by about 0.3%. The suppression effect of the CO_2–F on
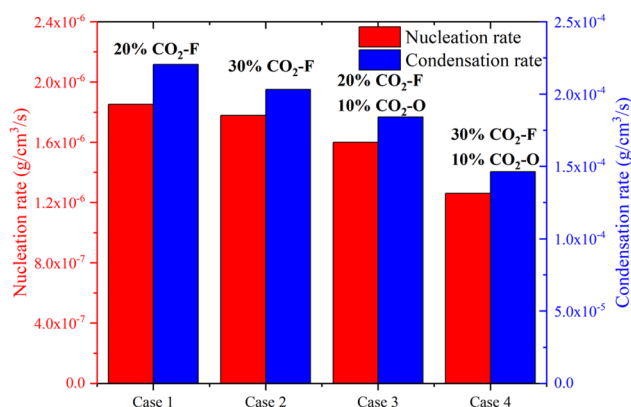

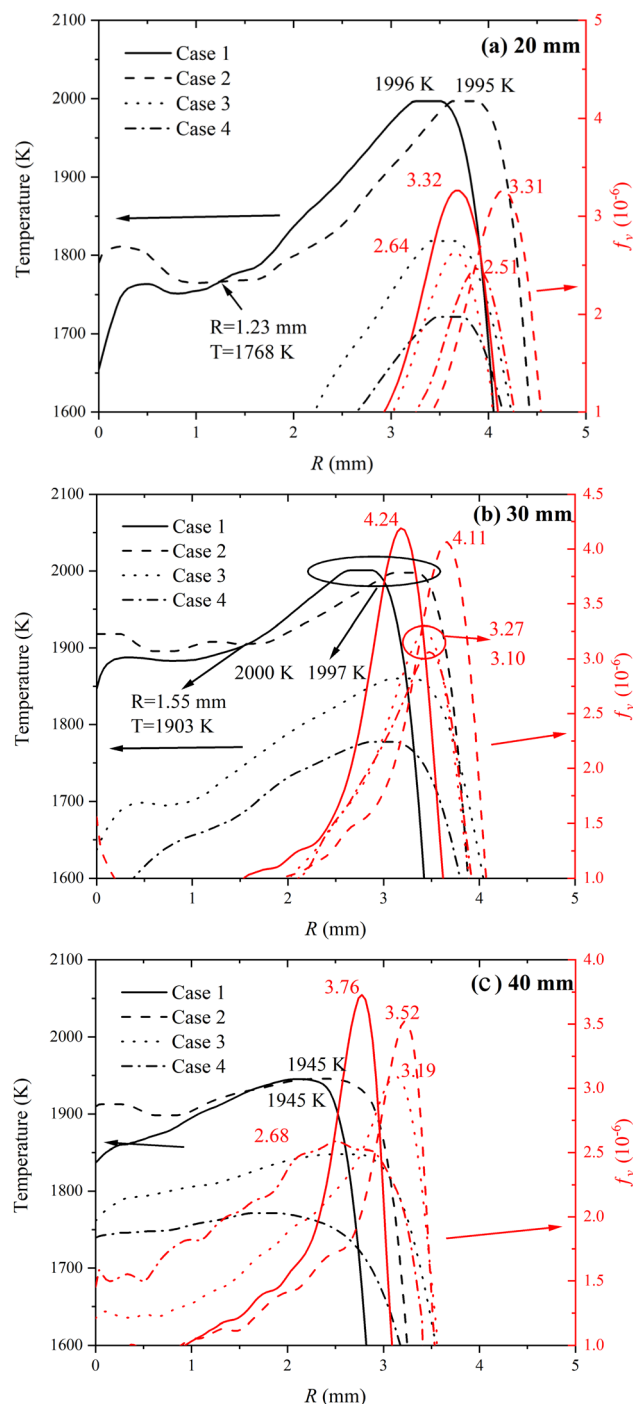Fig. 8 The soot nucleation and condensation rates for case 1 to case 4.

Fig. 9 Radical distributions of flame temperature and soot volume fraction from case 1 to case 4 at different heights (a) 20 mm, (b) 30 mm and (c) 40 mm.

soot formation was gradually evident with the increase of flame height. The peak soot volume fraction reduced by 3.07% and 6.38% at the flame heights of 30 mm and 40 mm, respectively, with the amount of the CO_2–F increasing from 20% to 30%. In the CO_2–F/O cases, the reductions in peak soot volume fraction were 4.92%, 5.2% and 16% caused by amount of the CO_2–F increasing from 20% to 30% at the flame height of 20 mm, 30 mm, and 40 mm, respectively.
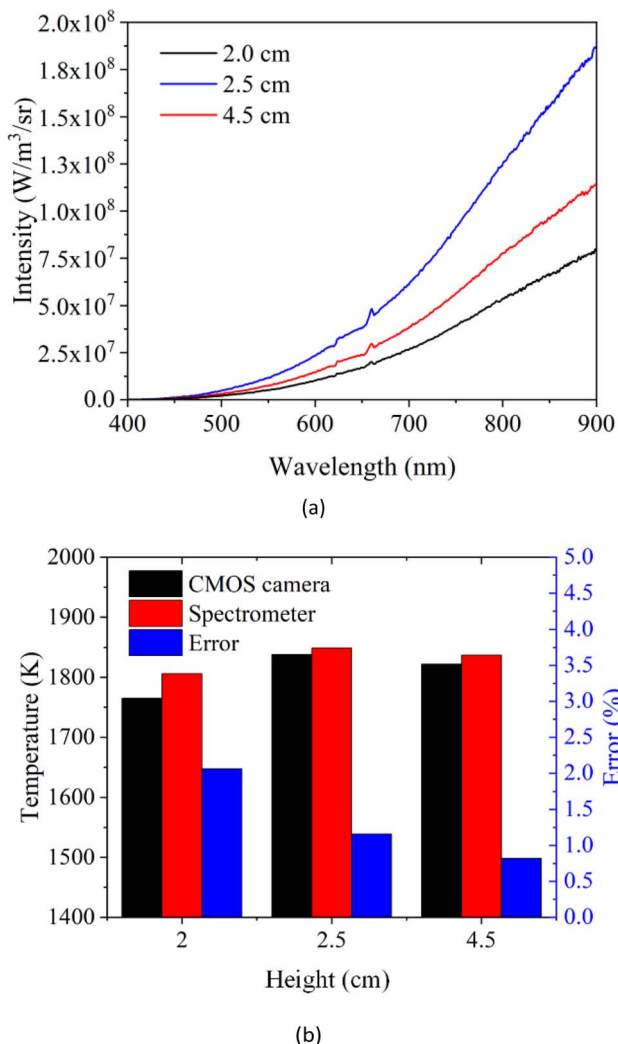
Fig. 10 (a) Radiation intensities measured by spectrometer. (b) Comparison of temperature measurement results between the spectrometer and CMOS imaging equipment.

In order to testify the accuracy of the flame temperatures measured by the CMOS imaging equipment, the radiation intensities at the heights of 2.0 cm, 2.5 cm and 4.5 cm along the flame central axis for the case 1 were measured by a calibrated spectrometer, as shown in Fig. 10a. The flame temperatures at different flame heights were then calculated by the measured radiation intensity employing the Levenberg–Malgorithm and the Hottel and Broughton emissivity model.[37] The results were compared in Fig. 10b. It could be seen that the temperatures obtained by the CMOS imaging equipment agreed well with the spectrometer measurements with the maximum relative errors was 2.48% at the flame height of 2 cm.

4. Conclusions

In this paper, experimental measurements were carried out in CO_2-diluted C_2H_4/air co-flow laminar diffusion flames to explore the effects of the CO_2–F, CO_2–O and CO_2–F/O on flame temperature and soot formation. The two-dimensional distributions of flame temperature and soot volume fraction were reconstructed based on the flame images obtained by the CMOS imaging equipment using the inverse Abel transform. To further understand the effects of CO_2 addition modes on suppression of soot formation, the flame temperature and soot volume fraction distributions along radius direction at different heights of flames were analyzed. The main conclusions are as follows.

(1) The effect of amount variation of the CO_2–F on the decrease of flame temperature was weaker than that of the CO_2–F/O. The decrease of the peak flame temperature in the CO_2–F cases was only 4 K, while the decrease of the peak flame temperature was 83 K in the CO_2–F/O cases. The effect of the CO_2–F on the decrease of flame temperature was mainly in the two wings region of the flame, the temperatures at the center axis of flame increased from 1785 K to 1866 K at the flame height of 5.5 cm in the CO_2–F cases.

(2) The soot formation was significantly suppressed by the effects of CO_2–F/O. The reductions in the peak soot volume fraction were 22.5% and 23.5% in the CO_2–F/O cases (20% CO_2–F 10% CO_2–O, 30% CO_2–F 10% CO_2–O) compared with the CO_2–F cases (20% CO_2–F, 30% CO_2–F). The height of soot formation region was affected by the combined effects of the CO_2–F and CO_2–O. The height of soot formation region was 1.8–3.7 cm in the CO_2–F cases, and height of soot formation region increased to 2.2–4.25 cm in the CO_2–F/O cases.

(3) In the CO_2–F cases, the flame temperature increased with the amount increase of CO_2–F at the central axis region of the flame, while in other areas (except the regions near the oxidizer side), the flame temperature decreased with the amount increase of CO_2–F, and coordinates of the demarcation points were 1.23 mm and 1.55 mm in radius, 30 mm and 40 mm in height, respectively. The flame temperature with 20% CO_2–F was higher than that with 30% CO_2–F in the CO_2–F/O cases.

(4) The suppression of soot formation caused by the CO_2–F was enhanced with the increasing flame height. In the CO_2–F cases, the peak soot volume fraction reduced only 0.3% at the flame height of 20 mm. The reductions in peak soot volume fractions were 3.07% and 6.38% at the flame heights of 30 mm and 40 mm, respectively. In the CO_2–F/O cases, the reductions in peak soot volume fraction were 4.92%, 5.2% and 16% at the flame height of 20 mm, 30 mm, and 40 mm, respectively.

Author contributions

The manuscript was written through contributions of all authors. All authors have given approval to the final version of the manuscript.

Conflicts of interest

The authors declare that there is no conflict of interest regarding the publication of this article.

Acknowledgements

References

1 R. Ahmad, Y. Zhou, C. Liang, G. Li, Z. Nan, A. Abbas, F. Yu, L. Li, J. Gong, D. Wang, Y. Yang, Z. Tang, M. Sultan, C. Sun and R. Dong, *RSC Adv.*, 2022, **12**, 20886–20896.

2 Z. Su, Y. Ying, C. Chen, R. Zhao, X. Zhao and D. Liu, *RSC Adv.*, 2022, **12**, 18181–18196.

3 S. S. Gill, J. Herreros, A. Tsolakis, D. Turner, E. Miller and A. York, *RSC Adv.*, 2012, **2**, 10400–10408.

4 R. Sui, J. Mantzaras and R. Bombach, *Proc. Combust. Inst.*, 2017, **36**, 4313–4320.

5 Y. Wang, X. Xue, H. Chen and G. Xu, *Front. Energy*, 2022, **16**, 307–320.

6 Q. Xu, K. Wang, J. Feng, C. Ding, C. Yu, Z. Du and Y. Zang, *J. Energy Eng.*, 2020, **146**, 04019041.

7 C. Li, Q. Z. Han, T. Zhu and W. Xu, *RSC Adv.*, 2020, **10**, 23491–23497.

8 R. Sui, W. Liang, J. Mantzaras and C. K. Law, *Combust. Flame*, 2020, **214**, 37–46.

9 C. A. Hoerlle, F. H. R. França, P. R. Pagot and F. M. Pereira, *Combust. Flame*, 2020, **217**, 294–305.

10 C. Zou, Y. Song, L. Guoyuan, C. Shiying, Y. He and C.-G. Zheng, *Int. J. Heat Mass Transfer*, 2014, **75**, 12–18.

11 Y. Wang, M. Gu, Y. Zhu, L. Cao, B. Zhu, J. Wu, Y. Lin and X. Huang, *Int. J. Hydrogen Energy*, 2021, **46**, 31400–31427.

12 K. P. Schug, Y. Manheimer-Timnat, P. Yaccarino and I. Glassman, *Combust. Sci. Technol.*, 1980, **22**, 235–250.

13 D. X. Du, R. L. Axelbaum and C. K. Law, *Symp. (Int.) Combust.*, 1991, **23**, 1501–1507.

14 F. Liu, H. Guo, G. J. Smallwood and Ö. L. Gülder, *Combust. Flame*, 2001, **125**, 778–787.

15 O. L. Gulder and M. F. Baksh, *Combust. Inst., Can. Sect.*, 1993, 1–5.

16 M. Frenklach, *Phys. Chem. Chem. Phys.*, 2002, **4**, 2028–2037.

17 F. Liu, H. Guo, G. Smallwood and Ö. Gülder, *Combust. Flame*, 2001, **125**, 778–787.

18 H. Guo and G. Smallwood, *Combust. Sci. Technol.*, 2008, **180**, 1695–1708.

19 J. Wu, L. Chen, P.-E. Bengtsson, J. Zhou, J. Zhang, X. Wu and K. Cen, *Combust. Flame*, 2019, **199**, 85–95.

20 Ö. L. Gülder and D. R. Snelling, *Combust. Flame*, 1993, **92**, 115–124.

21 M. Y. Choi, G. W. Mulholland, A. Hamins and T. Kashiwagi, *Combust. Flame*, 1995, **102**, 161–169.

22 N. Gupta, A. Sankaranarayanan, R. Sasidharakurup, A. Chowdhury and N. Kumbhakarna, *J. Aerosol Sci.*, 2021, **155**, 105773.

23 R. L. Vander Wal, *Combust. Flame*, 1998, **112**, 607–616.

24 R. L. Vander Wal, *Symp. (Int.) Combust.*, 1996, **26**, 2269–2275.

25 N. Jüngst and S. A. Kaiser, *Proc. Combust. Inst.*, 2021, **38**, 1089–1097.

26 Y. Wang and S. Chung, *Combust. Sci. Technol.*, 2016, **188**, 805–817.

27 M. Sirignano and A. D'Anna, *Exp. Therm. Fluid Sci.*, 2020, **114**, 110061.

28 P. Liu, Y. Zhang, L. Wang, B. Tian, B. Guan, D. Han, Z. Huang and H. Lin, *Energy Fuels*, 2018, **32**, 7112–7124.

29 Y. Ying and D. Liu, *Carbon*, 2018, 172–180.

30 C. Lou, Z. Li, Y. Zhang and B. M. Kumfer, *Combust. Flame*, 2021, **227**, 371–383.

31 F. Liu, A. E. Karataş, Ö. L. Gülder and M. Gu, *Combust. Flame*, 2015, **162**, 2231–2247.

32 L. Bowen, W. Chengjing, Z. Yindi, L. Bing, Z. Fanjin, S. Takyi and P. Tontiwachwuthikuld, *J. Energy Inst.*, 2022, **102**, 160–175.

33 Y. Tu, A. Zhou, M. Xu, W. Yang, K. B. Siah and P. Subbaiah, *Appl. Energy*, 2018, **220**, 962–973.

34 G. Legros, Q. Wang, J. Bonnety, M. Kashif, C. Morin, J.-L. Consalvi and F. Liu, *Combust. Flame*, 2015, **162**, 2705–2719.

35 Q.-x. Huang, F. Wang, D. Liu, Z.-y. Ma, J.-h. Yan, Y. Chi and K.-f. Cen, *Combust. Flame*, 2009, **156**, 565–573.

36 D. R. Snelling, K. A. Thomson, G. J. Smallwood, O. L. Guider, E. J. Weckman and R. A. Fraser, *AIAA J.*, 2002, **40**, 1789–1795.

37 S. Zheng, W. Cai, R. Sui, Z. Luo and Q. Lu, *Fuel*, 2022, **323**, 124328.